frontiers | Frontiers in Energy Research

TYPE Original Research
PUBLISHED 18 April 2024
DOI 10.3389/fenrg.2024.1399784

OPEN ACCESS

EDITED BY
Yuquan Zhang,
Hohai University, China

REVIEWED BY
Chongwei Zhang,
Dalian University of Technology, China
Shuangrui Yu,
University of Strathclyde, United Kingdom

*CORRESPONDENCE
Kang Ren,
✉ k.ren@ucl.ac.uk

RECEIVED 12 March 2024
ACCEPTED 02 April 2024
PUBLISHED 18 April 2024

CITATION
Sun SY, Gao R, Li Y and Ren K (2024), Hydrodynamic analysis of a floating platform integrated with buoys and spring components for energy conversion.
Front. Energy Res. 12:1399784.
doi: 10.3389/fenrg.2024.1399784

Hydrodynamic analysis of a floating platform integrated with buoys and spring components for energy conversion

Shi Yan Sun[1], Ruili Gao[1], Yueyang Li[1] and Kang Ren[2]*

[1]School of Naval Architecture and Ocean Engineering, Jiangsu University of Science and Technology, Zhenjiang, China, [2]Department of Mechanical Engineering, University College London, London, United Kingdom

Introduction: The study presents an integrated system comprising a central platform and four wave-energy converters, with a focus on investigating their coupled motions induced by ocean waves. The interaction between the buoys and the central platform is achieved through the implementation of spring components. The power take-off system is simulated by incorporating damping coefficients and stiffness into these spring components, enabling a detailed analysis of the energy conversion of such system.

Methods: Numerical simulations based on the continuity equation and the Reynolds-Averaged Navier-Stokes (RANS) equations, coupled with the realizable $k - \varepsilon$ turbulence model, are conducted. The two-phase flow model employs the Volume of Fluid (VOF) method to accurately capture free surface elevations. Additionally, frequency-domain predictions, based on the linearized velocity potential flow theory, are provided for a single central platform and buoy for comparative purposes.

Results: Detailed results regarding the effects of wave frequency and the damping coefficient of the power take-off system are presented.

Discussion: The results reveal that while both the platform's motion and the relative motions between buoys and the platform are suppressed, the absolute motion of buoys varies depending on their respective locations within the system and ocean waves. This variation is deeply influenced by the interaction between incident, reflected and diffracted waves within the system.

KEYWORDS

wave energy converter, coupled motion, PLATFORM, combined system, energy conversion

1 Introduction

Climate change is prompting governments worldwide to accelerate energy transitions. Oceans, covering 71% of the Earth's surface, are rich in solar, wind and wave energy. Consequently, developing offshore floating energy harvesting is expected to contribute significantly to net zero. So far, there have been many attempts to generate electricity by floating offshore ocean structures. However, the complex marine environment poses technical challenges to these activities, resulting in high costs and threatening equipment operations. The development of new floating platform solutions for hybrid renewable energy harvesting is expected to help reduce costs and improve safety.

An example of ocean-floating hybrid clean energy platform is developed by SINN Power. This innovative platform integrates various renewable energy sources, including solar, wind, and wave energy. Photovoltaic panels and small wind turbines are securely fixed to the truss structure of the floating platform. While prototype of hybrid power system is still scarce, extensive theoretical studies and experimental endeavours have been conducted. Sun et al. (2021) delved into the exploration of an array of heaving buoys encircling an A-shaped platform, employing both numerical simulations and experimental methods. They derived an optimization model by fine-tuning the spacing and arrangement of the buoys. Zheng and Zhang (2020) scrutinized the power performance, as well as the motion and pressure responses of a hybrid wave farm, incorporating oscillating water columns and point absorbers, utilizing a semi-analytical model. Their findings provided insights into the mooring type of oscillating water column (OWC), wave conditions, and the overall configuration of the farm. Cheng et al. (2022a) introduced a hybrid semi-submersible floating platform integrated with a flap-type wave energy converter and two oscillating buoys. Cheng et al. (2022b) proposed a novel concept: a hybrid wave energy conversion (WEC) and breakwater system combining an OWC and an oscillating buoy. Both experimental work and numerical simulations were conducted, and the results indicated a preference for the hybrid WEC concept, not only due to higher energy conversion but also for more robust wave attenuation. Further endeavours in this line of thought, including the combination of breakwater, oscillating buoy, and OWC, are being pursued by Lei et al. (2022), Cheng et al. (2022c) and Cheng et al. (2024). Cui et al. (2021) suggested a hybrid design featuring a cylindrical half-opening oscillating water column and a hinged oscillating buoy. Their research demonstrated that the hybrid system generally outperforms single OWC or single oscillating buoy in both frequency bandwidth and incident wave angle band. Nguyen and Wang (2020) utilized a linear power take-off system to connect a pontoon-type very large floating structure (VLFS) to the seabed. The wave energy is absorbed by the power take-off system through the motion of VLFS, achieving both wave energy extraction and a reduction in the hydroelastic response of the VLFS. Additionally, various studies explore energy extraction from the motion of VLFS, such as those by Nguyen et al. (2019) using a raft attachment, and Zhang et al. (2019) and Ren et al. (2019) by installing PTO systems between VLFS modules for extracting wave energy. Zhou et al. (2023a) contemplated a hybrid system involving a heaving cylindrical wave energy converter positioned in front of a parabolic breakwater. Furthermore, Zhou et al. (2023b) and Jin et al. (2023) delved into the wind-wave hybrid system, incorporating a floating offshore wind turbine alongside wave energy converters.

Numerical and experimental investigations into hybrid systems comprising platforms and wave energy converters are flourishing. However, the coupling between these components is not fully addressed in numerical analysis. Many studies focus on the coupling effect through hydrodynamic forces, accounting for the effects of both the motion of converters and the platforms. However, the power take-off system is typically applied solely to the wave energy converters, neglecting its direct impact on the platform. In offshore engineering, these components are interconnected rather than isolated. In the current work, we address this by incorporating spring components to establish a connection between the platform and oscillating buoys. The PTO system is simulated by introducing damping coefficients and stiffness to the springs. This approach allows the interaction force between the platform and oscillating buoys to be transmitted through the springs, with power being extracted accordingly. The spring force, in turn, depends on the relative motion between the platform and the spring. This nuanced understanding of coupling dynamics provides a more comprehensive insight into the interaction between platforms and wave energy converters in offshore engineering applications.

FIGURE 1
Visualization of the integrated energy system in the ocean.

2 Analysis of energy harvesting system

2.1 Configuration

Figure 1 illustrates a comprehensive floating energy system, featuring a floating semi-submersible platform with a concave wall, where the top surface can be mounted with solar photovoltaic panels, in addition to four spherical oscillating buoys around it. Each heaving buoy is linked to the central platform through two spring components, allowing for the utilization of suitable power take-off mechanisms to extract energy and convert it into electricity. The floating platform and heaving buoys are motivated by ocean waves, with their mutual dependence realized through the springs connecting them. In this study, we focus solely on analysing the heaving motions of the platform and four buoys, as well as their coupling effects through the spring components.

To better describe the integrated system, a Cartesian coordinate system is established with the origin O at the mass centre of the platform, also coinciding with the undisturbed water surface. The x-axis is along the direction of wave propagation, while the y-axis is perpendicular to it. The z-axis points upwards. The semi-submersible platform is featured as a solid of revolution with a concave wall. The illustration of the generatrix for the central platform is displayed in Figure 2. It has a radius R_{P1} at the top and the bottom, and at the waterline, the radius is R_{P2}. The curved part is a minor arc of a circle. This design approach enables the achievement of a compact waterplane, while also ensures sufficient space for the

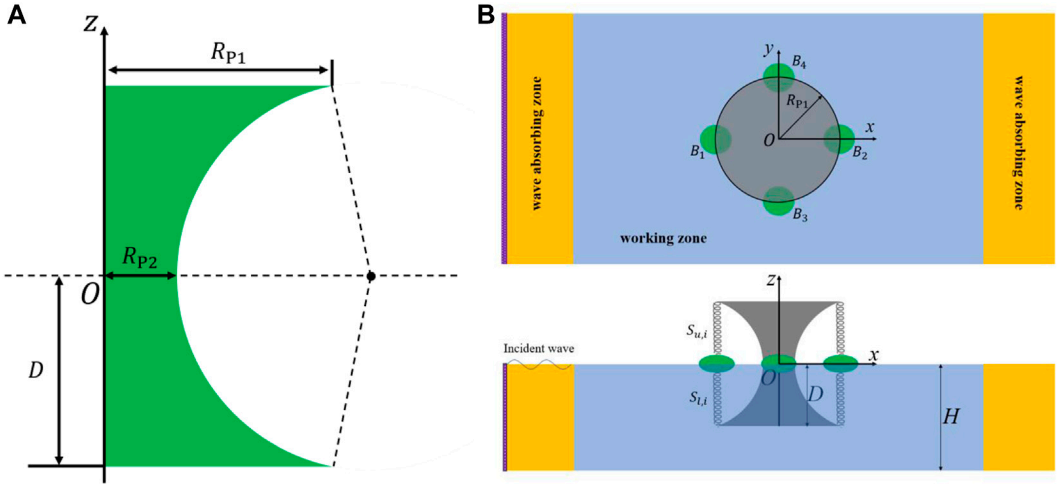

FIGURE 2
The illustration of **(A)** the generatrix for the central platform and **(B)** the top view and side view of the integrated system.

placement of components such as springs and buoys. In addition, the mean draught, equalling to the half-height of the platform, is denoted as D.

Four spheroid buoys with same geometry, denoted as $B_i\ (i = 1, 2, 3, 4)$, are positioned with their average centres evenly spaced on a circle with radius R_{P1} on the water surface, or $(x, y) = (R_{P1}, 0)$, $(-R_{P1}, 0)$, $(0, -R_{P1})$ and $(0, R_{P1})$, respectively. The equation of these spheroid is given as $(x^2 + y^2)/R_L^2 + z^2/R_H^2 = 1$, where R_L and R_H are the equatorial radius of the spheroid and the distance from the centre to the pole along the symmetry axis, respectively. The upper and lower spring components connected to B_i are denoted as $S_{u,i}$ and $S_{l,i}$, respectively, where the subscripts u and l refer to upper and lower. The seabed is assumed to be flat, and the average water depth is denoted as H.

2.2 Motion and energy extraction of the system

The motions of the heaving buoys $B_i\ (i = 1, 2, 3, 4)$ and the central platform are coupled through the forces due to the spring components, denoted as $F_{s,i}\,(i = 1, 2, 3, 4)$, and hydrodynamic forces. For each $F_{s,i}$, it includes the forces due to the upper spring $S_{u,i}$ and that of the lower spring $S_{l,i}$, which can be written as

$$F_{s,i} = -(b_{u,i} + b_{l,i})\left(\dot{h}_i - \dot{h}_p\right) - (k_{u,i} + k_{l,i})\left(h_i - h_p\right) \qquad (1)$$

where $b_{u,i}$ are the damping coefficients of the upper springs, and $b_{l,i}$ are those of the lower springs, and $k_{u,i}$ and $k_{l,i}$ are the stiffnesses of the upper and lower springs respectively. h_i and h_p are the vertical displacement of buoy B_i and the central platform respectively, the dot above h_i and h_p denotes the time derivative. Considering the effect of spring systems, the motion equation for each buoy B_i can be written as

$$m_i\ddot{h}_i + (b_{u,i} + b_{l,i})\left(\dot{h}_i - \dot{h}_p\right) + (k_{u,i} + k_{l,i})\left(h_i - h_p\right) = F_i,\ (i = 1 \sim 4) \qquad (2)$$

where m_i is the mass of the buoy B_i, and F_i is the hydrodynamic force exerted to the buoy B_i. The motion of the central platform can be written as

$$m_p\ddot{h}_p + \sum_{i=1}^{4}\left[(b_{u,i} + b_{l,i})\left(\dot{h}_p - \dot{h}_i\right) + (k_{u,i} + k_{l,i})\left(h_p - h_i\right)\right] = F_p, \qquad (3)$$

where m_p is the mass of the platform, and F_p is the fluid force exerted to the platform. Eqs (2) and (3) provide five equations in total, and they should be solved together to obtain the motions of four buoys and the central platform. In the coupling system, the average energy absorbed by one spring component may be expressed as

$$E_i = \frac{(b_{u,i} + b_{l,i})}{mT} \times \int_t^{t+mT} \left(\dot{h}_i - \dot{h}_p\right)^2 \mathrm{d}t, \qquad (4)$$

where m is positive integer and T refers to the period.

We further assume that the motion becomes sinusoidal with time with frequency ω, we may express $h_i - h_p = \mathrm{Re}(\beta_i e^{\mathrm{i}\omega t})$, where $\mathrm{i} = \sqrt{-1}$ and β_i is complex. From (4), we have

$$E_i = \frac{1}{2}(b_{u,i} + b_{l,i})\omega^2\xi_{i-p}^2. \qquad (5)$$

Here, $\xi_{i-p} = |\beta_i|$ is the average amplitude of the difference between the instantaneous motions of buoys and platform when the motion becomes stable. Here, we define ξ_i and ξ_p respectively as the motion amplitude of buoy B_i and the platform, we should note that ξ_{i-p} is unequal to $\xi_i - \xi_p$ due to phase difference of buoys and platform.

Due to the coupling of the motion of buoys and the platform, directly determining the optimal damping coefficients of the springs is challenging. However, these coefficients are crucial for identifying the most effective operational state of the comprehensive system. To address this, we simplify the scenario by using a system comprising one buoy and a spring pair to estimate the optimal damping coefficients for the spring components. In this simplified set-up, the upper and lower ends of the springs, initially connected to the platform, are assumed to be fixed in space. Meanwhile, we allow the single buoy with two springs to move in response to waves. This leads to $h_p = 0$ in Eq. (2), and the motion equation of a single buoy becomes

$$m\ddot{h} + (b_u + b_l)\dot{h} + (k_u + k_l)\dot{h} = F, \tag{6}$$

where h refers to the vertical displacement of a single buoy, and F is the external force from the fluid. Based on linearized velocity potential flow theory, F in (6) comprises wave exciting force f, wave radiation force and restoring force. Removing the radiation and restoring force terms to the left-hand side of Eq. 6, we have

$$(m + m_a)\ddot{h} + (b_a + b_u + b_l)\dot{h} + (k_a + k_u + k_l)h = f, \tag{7}$$

in which m_a and b_a are added mass coefficient and damping coefficient due to wave radiation, respectively. The parameter $k_a = \rho_w g \pi R_{P2}^2$ refers to the coefficient of restoring force of the buoy, in which g is the acceleration due to gravity. Similarly, we rewrite $h = \mathrm{Re}(\beta e^{i\omega t})$ and $f = \mathrm{Re}(f_0 e^{i\omega t})$, where β and f_0 are the complex amplitudes of motion of the buoy and wave exciting force respectively. Substituting these into Eq. 7, the motion amplitude ξ of the single buoy can be obtained as

$$\xi = |\beta| = \frac{|f_0|}{\sqrt{[(m + m_a)\omega^2 - (k_a + k_u + k_l)]^2 + (b_a + b_u + b_l)^2 \omega^2}}. \tag{8}$$

From (8), the natural frequency ω_n can be obtained as

$$\omega_n = \sqrt{\frac{k_a + k_u + k_l}{m + m_a}}. \tag{9}$$

Therefore, the mechanical energy E absorbed by the buoy per second takes the form of

$$E = \frac{b|f_0|^2}{2\left\{\left[(m + m_a)\omega - \frac{(k_a + k_u + k_l)}{\omega}\right]^2 + (b_a + b)^2\right\}}, \tag{10}$$

where $b = b_u + b_l$. Applying $\frac{\partial E}{\partial b} = 0$, the optimal damping coefficient b_{opt} can be obtained as

$$b_{\mathrm{opt}} = \sqrt{\frac{[(m + m_a)\omega^2 - (k_a + k_u + k_l)]^2}{\omega^2} + b_a^2}. \tag{11}$$

3 Numerical model

To obtain the values of hydrodynamic variables mentioned in Section 2.2, the interaction between ocean waves and the comprehensive floating energy harvesting system is examined in the numerical tank. The continuity equation and RANS equations for an incompressible Newtonian fluid can be expressed in the Einstein notation in Cartesian coordinate system as follows

$$\frac{\partial \bar{u}_i}{\partial x_i} = 0, \tag{12}$$

$$\frac{\partial \rho \bar{u}_i}{\partial t} + \bar{u}_j \frac{\partial \rho \bar{u}_i}{\partial x_j} = -\frac{\partial \bar{p}}{\partial x_i} + \bar{f}_i + \mu \frac{\partial^2 \bar{u}_i}{\partial x_j \partial x_j} - \frac{\partial \rho \overline{u_j' u_i'}}{\partial x_j}, \tag{13}$$

TABLE 1 Spheroid types with different parameters.

Spheroid type	R_H (m)	R_L (m)
Oblate spheroid	0.228	0.456
Sphere	0.372	0.372
Prolate spheroid	0.574	0.287

where t is time, ρ is the density of the fluid, μ is the dynamic viscosity of fluid, the overbar means the time average. Both subscript indexes i and j correspond to the directions of (x, y, z). u_i are the velocity components and f_i are mass forces. p is the pressure of the viscous flow. A realizable $k - \varepsilon$ model (Shih et al., 1995a; Shih et al., 1995b) is used to establish the relationship between the Reynolds stress and average velocity. A volume of fluid (VOF) method is used to capture the free surface elevation in the two-phase flow model, and the volume fraction α is described as the ratio of the water volume to the total volume in a cell. Then density of two-phase fluid including air and water can be expressed as

$$\rho = \rho_w \alpha + \rho_a (1 - \alpha). \tag{14}$$

The use of Eq. 14 can transform the equation of ρ to that with respect to fraction α. When α is obtained, the free surface would be captured.

As displayed in Figure 2B, the numerical tank is divided into two kinds of zones: the working zone and the wave-absorbing zone. Boundary conditions in the 3D computational domain are configured as follows: the left-hand side boundary is specified as a velocity inlet, generating the fifth-order Stokes incident waves. The right-hand side boundary is set as a pressure outlet. Tank lateral surfaces are designated as symmetry boundaries, and the bottom is modelled as a wall boundary. On the domain's top, a velocity inlet boundary condition is used. To mitigate reflected and diffracted waves propagating to the inlet and outlet, a forcing method is employed in wave-absorbing zone.

4 Results and analysis

4.1 The shape of heaving buoy

To select the appropriate geometric shape for the buoy, we may utilize Eqs. 10 and (11) for an approximate estimation. In these equations, the hydrodynamic coefficients such as the added mass m_a, damping coefficient b_a, and the amplitude of wave exciting force $|f_0|$ can be obtained through linear analysis using software ANSYS-AQWA. Three spheroids of different parameters are chosen and displayed in Table 1, respectively correspond to an oblate spheroid, a sphere, and a prolate spheroid.

They have the same mass, which is $m = 99.129$kg. For simplification, the properties of the spring systems are assumed the same. The damping coefficients of the upper and lower springs are set as $b_u = b_l = 0.5b_{\mathrm{opt}}$, where b_{opt} can be calculated from Eq. 11. The stiffnesses of the upper and lower springs are $k_u = k_l = 500$N/m. For these three spheroids, the motion amplitude per wave amplitude and absorbed energy capacity, defined as energy absorbed per second per body mass per wave amplitude, are respectively

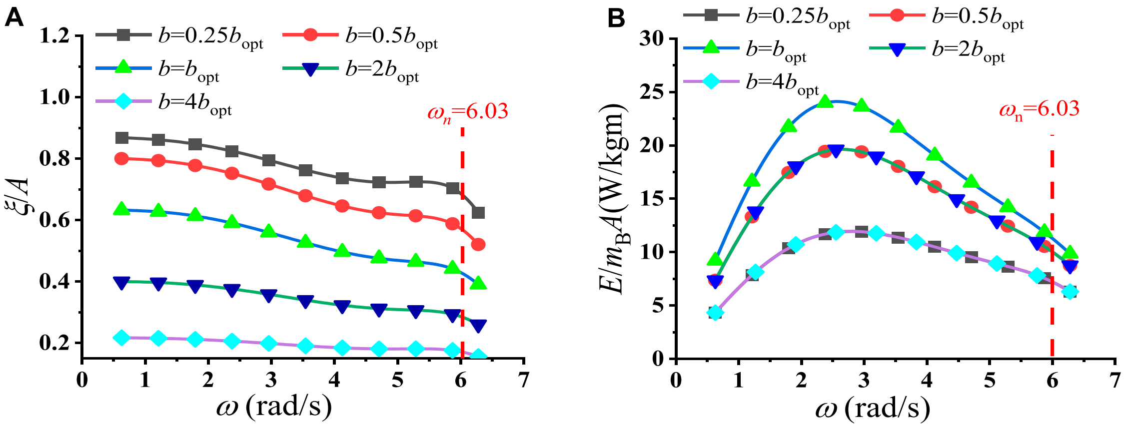

FIGURE 3
Frequency-domain analysis for an oblate spheroid: **(A)** motion amplitude per wave amplitude and **(B)** absorbed energy per second per body mass per wave amplitude.

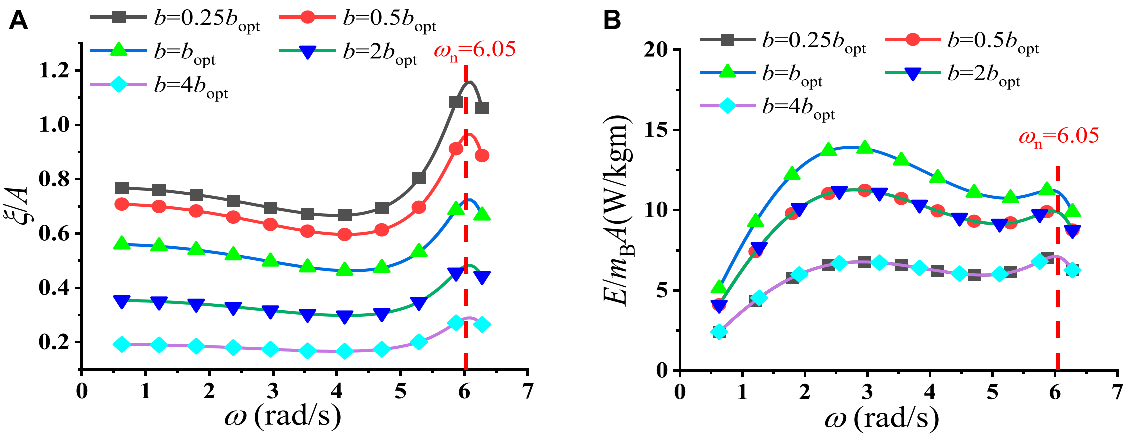

FIGURE 4
Frequency-domain analysis for a sphere: **(A)** motion amplitude per wave amplitude and **(B)** absorbed energy per second per mass per wave amplitude.

plotted against wave frequencies in Figures 3, 4, 5 for an oblate spheroid, a sphere and a prolate spheroid. In these three cases, the added mass m_a are calculated through linear hydrodynamic analysis and substituted into Eq. 9 to work out the natural frequency ω_n, namely, $\omega_n \approx 6.03$ rad/s, 6.05 rad/s and 5.48 rad/s respectively for the oblate spheroid, sphere and prolate spheroid, as marked by the red dashed vertical lines in Figures 3–5.

We may investigate these curves further. According to Eq. 8, it can be observed that if the term $(b_a + b_u + b_l)^2\omega^2$, which relates to the damping force of the spring, is negligible, the motion amplitude ξ would reach its maximum when the wave frequency is equal to the natural frequency, indicating resonance. This is evident in the sphere and prolate spheroid cases, as shown in Figure 4A and 5A, where the greatest motion amplitude is observed near $\omega = \omega_n$. In addition, as shown in Figure 5B, the maximum energy capacity is also concentrated at the resonance frequency for the prolate spheroid case. However, in the case of the sphere, as illustrated in Figure 4B, there is only a minor energy peak near $\omega = \omega_n$, while the significant peak appears at $\omega \approx 2.5$ rad/s. This can also be elucidated by Eq. 10, where if the term $\left[(m + m_a)\omega - \frac{(k_a+k_u+k_l)}{\omega}\right]^2$ and the hydrodynamic damping coefficient b_a are both small, then the energy E primarily depends on $|f_0|^2/b_{\text{opt}}$. For the sphere, the peak of $|f_0|^2/b_{\text{opt}}$ occurs at $\omega \approx 2.8$ rad/s, thus the largest energy capacity is observed near this frequency.

For the oblate spheroid case, as the damping force of spring is noticeably important than other force components, the energy peak mainly depends on the peak of $|f_0|^2/b_{\text{opt}}$, the largest energy is at $\omega \approx 2.5$ rad/s, and the effect of resonance is not prominent in this case, as illustrated in Figure 3. It may be worth noting that, in practice, high absorbed energy in lower wave frequency is expected, and this is for a more energy would be absorbed from the wave with a larger wavelength relative to the size of body. Thus, in the following work, we use the

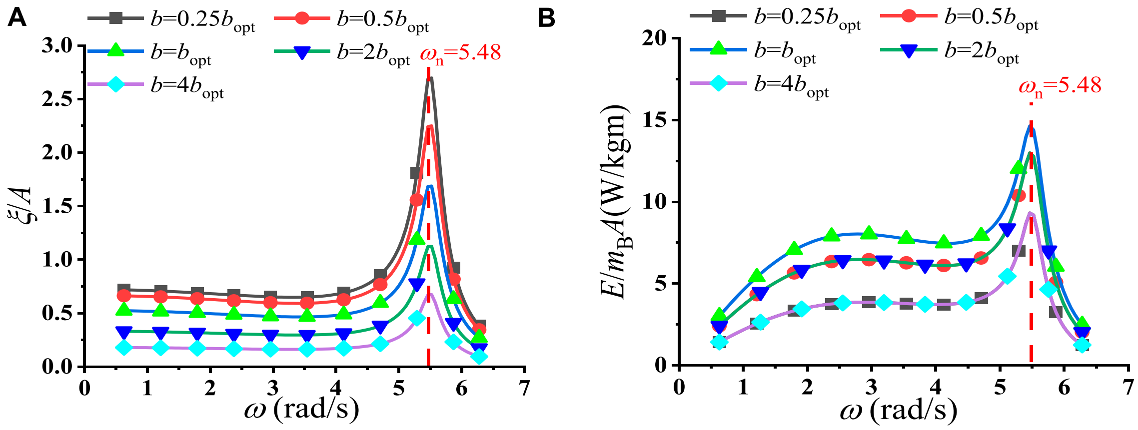

FIGURE 5
Frequency-domain analysis for a prolate spheroid: **(A)** motion amplitude per wave amplitude and **(B)** absorbed energy per second per mass per wave amplitude.

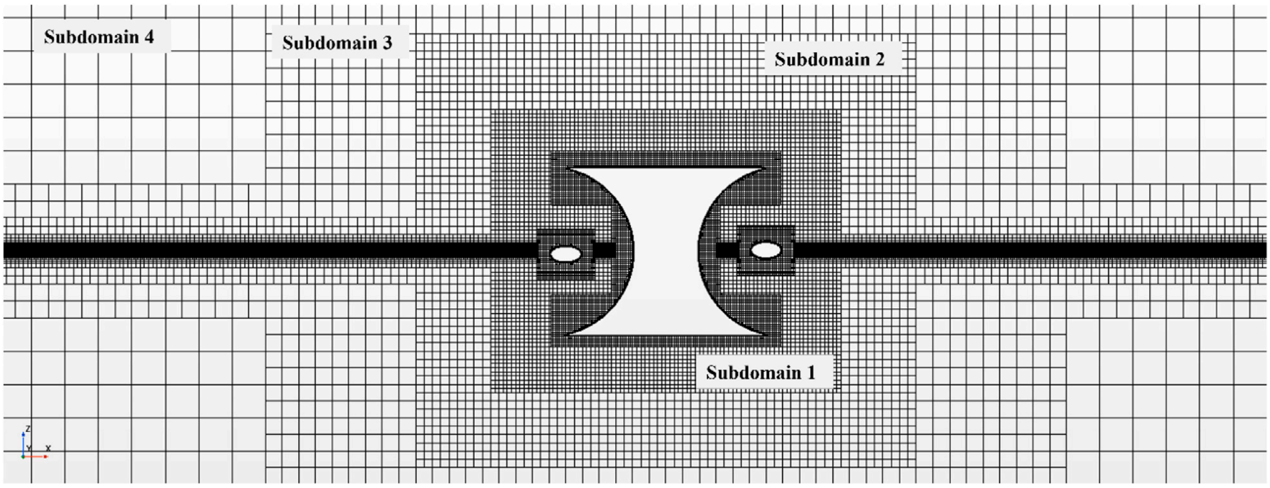

FIGURE 6
Trimmed mesh for the computational domain.

oblate spheroid, with the coefficients $R_H = 0.228\text{m}$ and $R_L = 0.456\text{m}$, to consider the coupling effect of the combined system.

4.2 Nonlinear numerical setup and convergence study

The time-domain simulation of wave interaction with the integrated system is conducted. Four oblate spheroid buoys with identical geometries, as outlined in Table 1, along with a floating platform with dimensions $R_{P1} = 3\text{m}$, $R_{P2} = 0.95\text{m}$ and $D = 2.5\text{m}$. The radius of the concave wall of the platform is set as 2.55 m. A cubic computational domain is adopted for the simulation. For each wave frequency, the length of the computational domain is set at 8λ, and the length of the wave-absorbing zone at both ends of the domain is configured to be 2λ. In addition, the domain width is fixed at 16m, and the water depth at 10 m.

The convergence study is conducted based on a case study where the circular radian frequency ω of the incident wave is set at 2.512 rad/s, and the corresponding wavelength, denoted as λ, is 9.8 m. The wave height is fixed at $H_W = 0.15\text{m}$. The damping coefficients of the springs are set as $b_u = b_l = b_{\text{opt}}/2$. In the present case, $b_{\text{opt}} = 2169\text{N}\cdot\text{s/m}$. The stiffnesses of the upper and lower springs are set to $k_u = k_l = 500\text{N/m}$, as in Section 4.1.

Trimmed meshes are used to discretize the entire computational domain. To account for the motion of bodies, an overset mesh approach is employed. Within the overset domain, the finer mesh relative to the body size is utilized. To enhance numerical efficiency, a multi-block grid has been used. Finer meshes are adopted to regions within the overset domain and in close proximity to the free surface. For example, the region close to the free surface is encrypted four times in z direction. The remaining domain is divided into four subdomains, as illustrated in Figure 6. Mesh sizes within subdomain 1, 2, 3 and 4 are established as $2l_0$, $4l_0$, $8l_0$, and $16l_0$, respectively. For

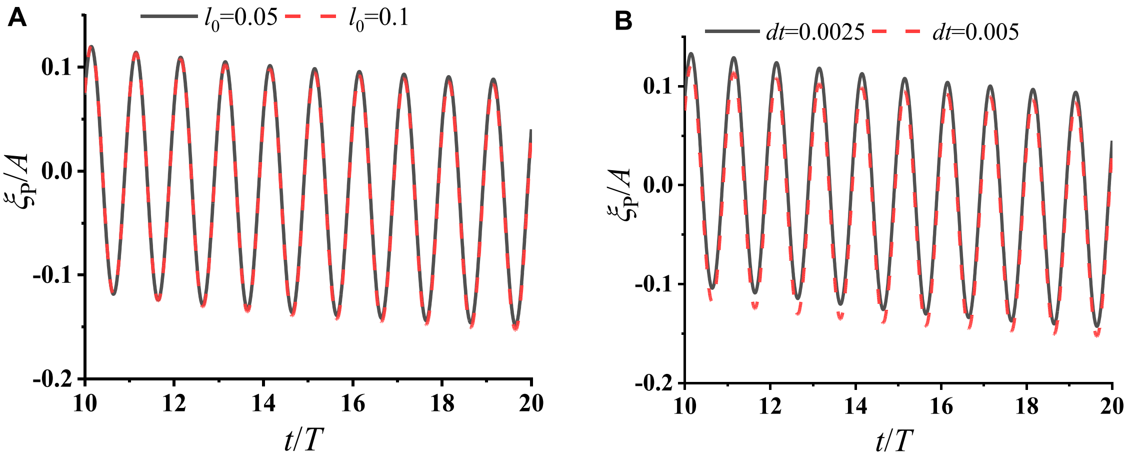

FIGURE 7
Convergence study for the motion amplitude of the central platform with respect to **(A)** mesh and **(B)** time step.

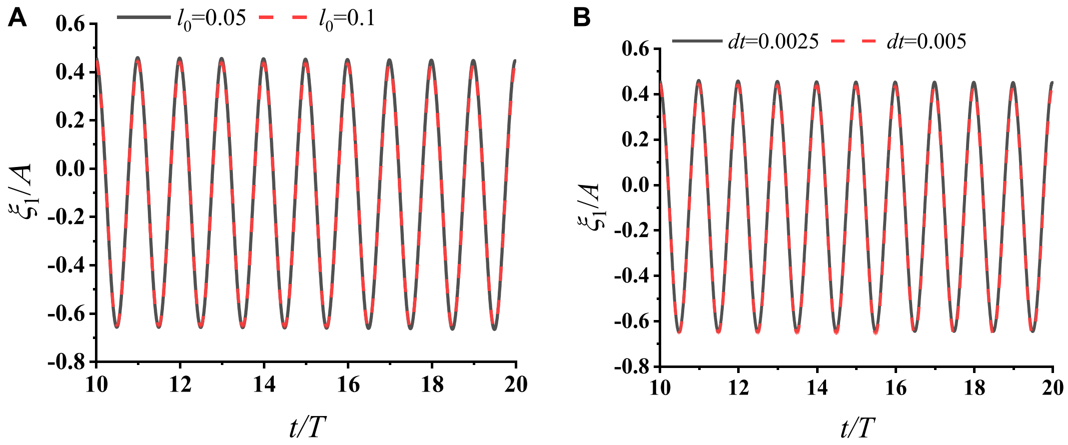

FIGURE 8
Convergence study for the motion amplitude of the buoy B_1 with respect to **(A)** mesh and **(B)** time step.

mesh convergence analysis, two sets of grid lengths are considered as basis, namely, $l_0 = 0.05$ m and 0.1m, respectively.

In addition, time step (dt) is set at 0.005s and 0.0025s, respectively. Figure 7 presents the studies of the mesh convergence and time step convergence for the vertical motion of platform in the integrated system, while Figure 8 depicts those for buoy 1. Similar convergence results are observed for Buoys 2 to 4 and hence only the results of buoy 1 are provided. The good agreement seen in Figure 7 and 8 verifies that the present procedure is dependent of both time and mesh. Subsequently, simulations were conducted using $l_0 = 0.01$m and $dt = 0.005$s in the following sections.

4.3 The effect of incident wave frequencies

In this section, we explore the impact of incident wave frequencies. The parameters of the buoys and the central platform remain consistent with those utilized in the convergency study, despite being subjected to varying wave frequencies. Specifically, six wave frequencies are selected as 0.628 rad/s^{-1}, 1.256 rad/s^{-1}, 1.884 rad/s^{-1}, 2.512 rad/s^{-1}, 3.14 rad/s^{-1} and 3.768 rad/s^{-1}, with a fixed wave height of $H_W = 0.15$m.

The optimal damping coefficient, b_{opt}, varying with the wave frequency ω, is calculated using Eq. 9. In the present numerical simulation, the setting of b_{opt} can be achieved by setting the damping coefficients of the two spring pairs corresponding to B_i as $b_{u,i} = b_{l,i} = b_{opt}/2$. The stiffness of the springs should be set as positive constants, reflecting the capacity to restore energy. In Eq. 13, it is evident that increasing the stiffness raises the natural frequency of the system, which does not favour the absorption of energy in the low frequency region. Therefore, we assign a smaller value to the stiffness, setting $k_{u,i} = k_{p,i} = 500$N/m.

Figure 9A illustrates a comparison of the prediction of the motion amplitudes between a single platform analysed in the frequency domain using linearized potential flow theory and the platform coupled with springs and buoys in the integrated

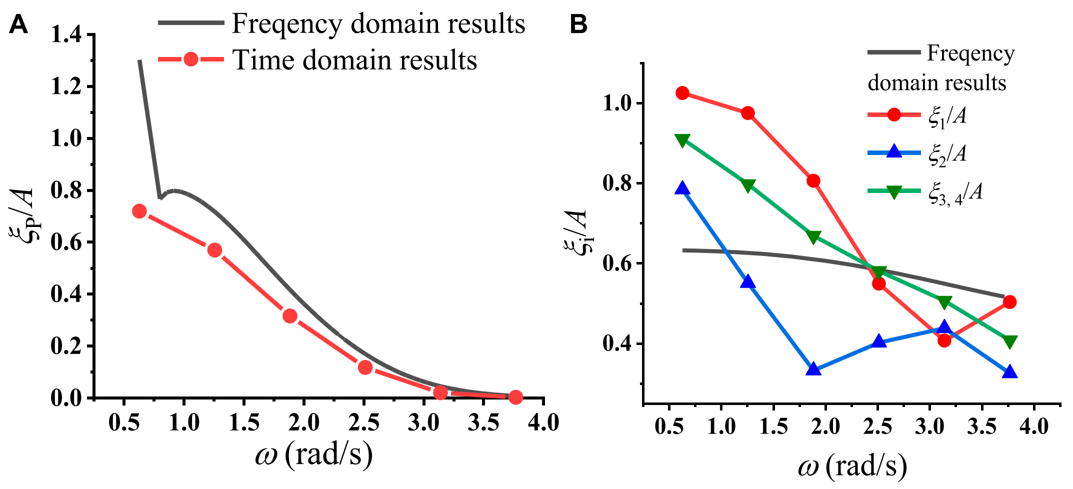

FIGURE 9
(A) The motion of platform and **(B)** absolute motion amplitudes ξ_i of buoys at different wave frequencies ω.

system, as analysed in the time domain simulation based on Reynolds-Averaged Navier-Stokes (RANS) equations. The latter one is obtained through a long-time simulation to achieve its steady state. It is observed that the motion amplitudes of platform in the integrated system are generally smaller than those of a single platform in the frequency-domain simulation. This discrepancy may be attributed to several factors. First, the inclusion of buoys alters the mass of the entire system, along with added mass and wave-exciting forces. In addition, a portion of the wave energy is absorbed by the wave energy converters surrounding the platform, leading to a reduction in platform motion. As the wave frequency increases, the motion amplitudes for both cases gradually diminish. It is expected that as the wavelength becomes very short, numerous wave elements will surround the bodies, potentially resulting in the cancellation of the hydrodynamic effects.

In addition to the central platform, Figure 9B illustrates the motion amplitudes of the four buoys in the coupled system, along with the motion amplitude of the single buoy in frequency domain based on linearized analysis. As the symmetry of the positions of B_3 and B_4 corresponding to the incident waves and the central platform, their results coincide with each other. From the figure, we can observe that for wave frequencies other than $\omega = 2.512$ rad/s and 3.14 rad/s, the motion amplitude of B_1, situated at the upstream side of the platform, is the largest. Those at the two sides are smaller but still larger than that in the frequency-domain prediction, and the one at the downstream. However, at $\omega = 2.512$ rad/s and 3.14 rad/s, the motion amplitude of the single buoy in the frequency-domain prediction is the largest. The motion of the buoy B_1 is smaller than the buoys at the two sides, and at $\omega = 3.14$ rad/s, it is even smaller than that of B_2 at the downstream side.

This observation appears to contradict the intuition that the motion amplitude of buoy B_1 should be largest, as it directly faces the incoming waves, thus experiencing the direct impact of wave energy. While this holds true in many cases, it is important to notice that waves can also be reflected by the central platform. If the incident wave interacts with the reflected wave, the wave energy or wave height in front of the central platform may diminish. Consequently, a significant portion of energy may either propagate to the back through bypassing the platform or forming diffracted waves. Thus, we could see the motion of B_1 is smallest at $\omega = 3.14$ rad/s. Below $\omega = 2.512$ rad/s, the motion amplitudes of buoys B_1, B_3 and B_4 are larger than those of frequency domain, the reason for this is because among these frequencies, the reflected wave and incident wave are not fully cancelled by each other, they both take positive effects on the motion of buoys.

From the previous analysis and Eq. 5, it becomes evident that the relative motion between the platform and buoy B_i, or ξ_{i-p} $(i = 1, 2, 3, 4)$, is crucial for energy absorption. Consequently, Figure 10 illustrates ξ_{i-p} and the corresponding energy capacities, defined as energy absorbed per body mass per wave amplitude, for each buoy B_i. In the four wave frequencies other than $\omega = 2.512$ rad/s and 3.14 rad/s, the relative motion of B_1 corresponding to the central platform is larger than that of the other buoys. It remains to be smaller than the motion of the single uncoupled buoy in the frequency-domain prediction. It might be worth noting that ξ_3 exhibits significant differences compared to ξ_2 in these wave frequencies, while ξ_{3-p} appears close to ξ_{2-p} as shown in Figure 10A. This disparity can be attributed to the phase difference among the buoys.

At $\omega = 2.512$ rad/s and 3.14 rad/s, the relative motion of B_1, or ξ_{1-p}, is no longer the largest. This can be due to the offset between the incident wave and the reflected wave. Overall, the differences in relative motions among buoys are much smaller than those in absolute motions. In other words, while each buoy in the integrated system shows distinct motion characteristics, their motions relative to the central platform are closer due to the coupling effect of the system. The absorbed energy, directly related to the relative motion, follows a similar variation trend. Both relative amplitude and absorbed energy are smaller than the results of a single uncoupled buoy in the frequency domain. This reduction in absorbed energy can be attributed to the change of wave energy distribution caused by the platform within the coupled system.

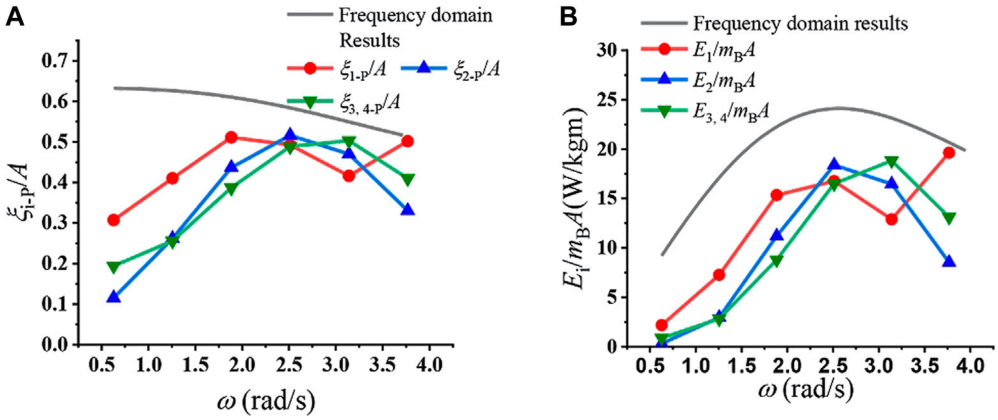

FIGURE 10
(A) Relative motion of buoys and **(B)** absorbed energy of the combined system at different wave frequencies.

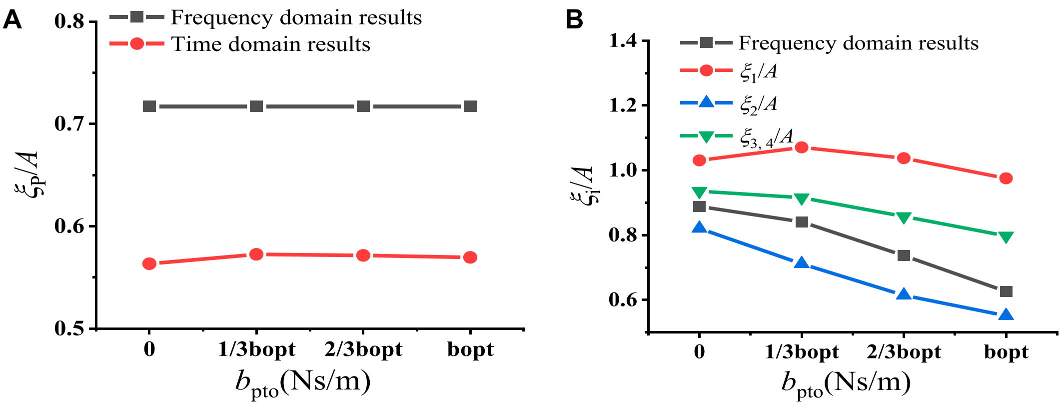

FIGURE 11
(A) The motion of platform and **(B)** absolute motion amplitudes ξ_i of buoys at different damping coefficients b_{pto}.

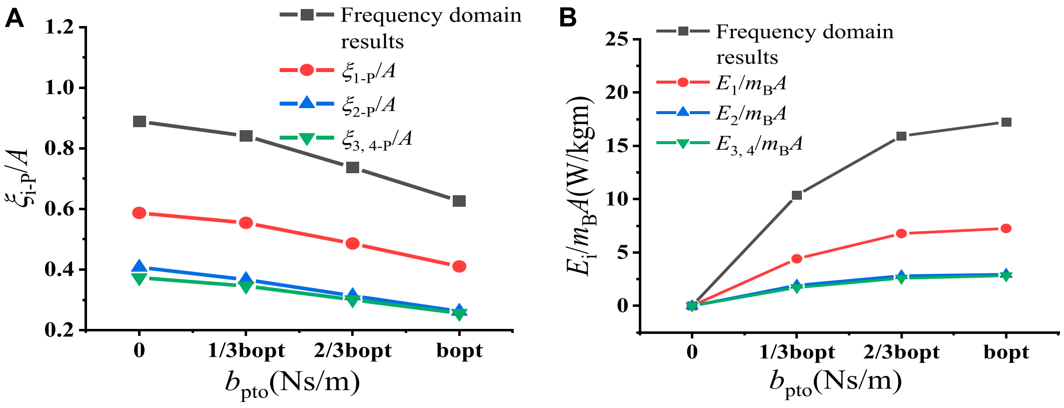

FIGURE 12
(A) Relative motion of buoys and **(B)** absorbed energy of the combined system at different damping coefficients b_{pto}.

4.4 The effect of damping coefficient

Figure 11 presents the results obtained with different damping coefficients. Specifically, b_{pto} is varied as 0, $b_{opt}/3$, $2b_{opt}/3$ and b_{opt}, which can also be achieved by simply setting $b_{u,i} = b_{l,i} = b_{pto}/2$. In the present study case, we maintain $k_{u,i} = k_{p,i} = 500\text{N/m}$, with a wave frequency of $\omega = 1.256$ rad/s and a wave height of $H_{\text{W}} = 0.15\text{m}$.

Figure 11A illustrates the motion of the platform in the frequency-domain analysis without buoys and the time-domain analysis integrated system coupled with buoys, with the latter exhibiting smaller motion response compared to the former. One reason for this discrepancy is the absorption of wave energy by the surrounding buoys, while another factor is the alteration of the system's dynamic performance due to the increased mass, added mass etc. However, it is noteworthy that the variation in platform motion with changes in the springs' damping coefficient is not significant. Therefore, we can conclude that the variation in the dynamic performance of the system exerts more profound effects on the motion of the platform. Figure 11B displays the absolute motion amplitudes of the buoys, and the frequency-domain prediction of a single buoy is also displayed for comparison. Among the buoys, B_1 exhibits the largest motion, followed by B_3 and B_4, and B_2 with the smallest motion. The frequency-domain prediction results for the single buoy fall between B_2 and B_3 or B_4. These variations can be due to the interaction between incident waves, radiation waves, and diffracted wave, as previously discussed.

The relative motion results are illustrated in Figure 12A, with B_2, B_3 and B_4 closely aligned, while B_1 exhibits greater movement. This trend is mirrored in the energy distribution displayed in Figure 12B. As the value of b_{pto} increases, both absolute motion and relative motion decrease, while the absorbed energy increases. At $b_{pto} = b_{opt}$, the energy reaches the peak. This suggests that the optimal damping coefficient obtained from the single buoy based on the frequency-domain analysis can be used to the prediction of the optimal damping coefficient for the integrated system.

5 Conclusion

A coupled energy harvesting system including the central platform, oscillating buoys and spring components are proposed in present work. Specifically, the power take-off system is simulated by introducing damping coefficients and elastic coefficients to the spring components. The Reynolds-Averaged Navier-Stokes (RANS) equation and realizable $k - \varepsilon$ model are used for the problem, and following conclusions are drawn.

(1) The motion of the platform in the coupled system is lower than that of a single platform. It can be explained that the addition of buoys alters the dynamic performance of the system, such as increasing mass, added mass and wave exciting force. Additionally, a portion of wave energy would be absorbed by the buoys surrounding the platform.
(2) The variation in platform motion across different damping coefficients in the coupled system is not significant. This implies that the changes in the dynamic performance of the system have a more noticeable effect on the motion of platform than the energy absorption of buoys.
(3) The absolute motion of buoys is primarily influenced by the interaction of incident, reflected and diffracted waves, when the incident wave and reflected wave are cancelled at the front of the platform, the motion amplitude of buoy at this location will drop, while when most of waves are diffracted around the platform, the buoys at two sides and the back will undertake larger motions.
(4) In the couple system, the relative motions between buoys are closer than absolute motions. The absorbed energy, which is directly related to the relative motion, also shows a similar variation trend.

Data availability statement

The original contributions presented in the study are included in the article/supplementary material, further inquiries can be directed to the corresponding author.

Author contributions

SS: Writing–original draft, Writing–review and editing, Funding acquisition. RG: Writing–original draft. YL: Writing–review and editing. KR: Writing–original draft, Writing–review and editing.

Funding

The author(s) declare that financial support was received for the research, authorship, and/or publication of this article. This work is supported by the Royal Society (Grant No. IEC\NSFC\223358) and the National Natural Science Foundation of China (Grant No. 52271276).

Conflict of interest

The authors declare that the research was conducted in the absence of any commercial or financial relationships that could be construed as a potential conflict of interest.

Publisher's note

References

Cheng, Y., Dai, S. Q., Dai, S. S., Ji, C. Y., Collu, M., Yuan, Z. M., et al. (2022a). Energy conversion and hydrodynamic analysis of multi-degree-of-freedom wave energy converters integrated into a semi-submersible platform. *Energy Convers. Manag.* 252, 115075. doi:10.1016/j.enconman.2021.115075

Cheng, Y., Fu, L., Dai, S. S., Collu, M., Cui, L., Yuan, Z. M., et al. (2022b). Experimental and numerical analysis of a hybrid WEC-breakwater system combining an oscillating water column and an oscillating buoy. *Renew. Sustain. Energy Rev.* 169, 112909. doi:10.1016/j.rser.2022.112909

Cheng, Y., Fu, L., Dai, S. S., Collu, M., Ji, C. Y., Yuan, Z. M., et al. (2022c). Experimental and numerical investigation of WEC-type floating breakwaters: a single-pontoon oscillating buoy and a dual-pontoon oscillating water column. *Coast. Eng.* 177, 104188. doi:10.1016/j.coastaleng.2022.104188

Cheng, Y., Song, F. K., Fu, L., Dai, S. S., Yuan, Z. M., and Incecik, A. (2024). Experimental investigation of a dual-pontoon WEC-type breakwater with a hydraulic-pneumatic complementary power take-off system. *Energy* 286, 129427. doi:10.1016/j.energy.2023.129427

Cui, L., Zheng, S. M., Zhang, Y. L., Miles, J., and Iglesias, G. (2021). Wave power extraction from a hybrid oscillating water column-oscillating buoy wave energy converter. *Renew. Sustain Energy Rev.* 135, 110234. doi:10.1016/j.rser.2020.110234

Jin, P., Zheng, Z., Zhou, M., Zhou, B. Z., Wang, L., Yang, Y., et al. (2023). Optimization and evaluation of a semi-submersible wind turbine and oscillating body wave energy converters hybrid system. *Energy* 282, 128889. doi:10.1016/j.energy.2023.128889

Lei, F., and Cheng, Y. (2022). Hydrodynamic performance of A dual-floater integrated system combining hybrid WECs and floating breakwaters. *China Ocean. Eng.* 36, 969–979. doi:10.1007/s13344-022-0085-9

Nguyen, H. P., and Wang, C. M. (2020). Heaving wave energy converter-type attachments to a pontoon-type very large floating structure. *Eng. Struct.* 219, 110964. doi:10.1016/j.engstruct.2020.110964

Nguyen, H. P., Wang, C. M., Flocard, F., and Pedroso, D. M. (2019). Extracting energy while reducing hydroelastic responses of VLFS using a modular raft wec-type attachment. *Appl. Ocean Res.* 84, 302–316. doi:10.1016/j.apor.2018.11.016

Ren, N. X., Zhang, C., Magee, A. R., Hellan, Ø., Dai, J., and Ang, K. K. (2019). Hydrodynamic analysis of a modular multi-purpose floating structure system with different outermost connector types. *Ocean. Eng.* 176, 158–168. doi:10.1016/j.oceaneng.2019.02.052

Shih, T. H., Liou, W. W., Shabbir, A., Yang, Z., and Zhu, J. (1995a). A new k-ϵ eddy viscosity model for high Reynolds number turbulent flows. *Comput. Fluids* 24 (3), 227–238. doi:10.1016/0045-7930(94)00032-t

Shih, T. H., Zhu, J., and John, L., (1995b). A new Reynolds stress algebraic equation model. *Comput. Methods Appl. Mech. Eng.* 125, 287–302. doi:10.1016/0045-7825(95)00796-4

Sun, P. Y., Hu, S., He, H. Z., Zheng, S. G., Chen, H., Yang, S. H., et al. (2021). Structural optimization on the oscillating-array-buoys for energy-capturing enhancement of a novel floating wave energy converter system. *Energy Convers. Manag.* 228, 113693. doi:10.1016/j.enconman.2020.113693

Zhang, X. T., Zheng, S. M., Lu, D., and Tian, X. L. (2019). Numerical investigation of the dynamic response and power capture performance of a VLFS with a wave energy conversion unit. *Eng. Struct.* 195, 62–83. doi:10.1016/j.engstruct.2019.05.077

Zheng, S. M., Zhang, Y. L., and Iglesias, G. (2020). Power capture performance of hybrid wave farms combining different wave energy conversion technologies: the H-factor. *Energy* 204, 117920. doi:10.1016/j.energy.2020.117920

Zhou, B. Z., Wang, Y., Zheng, Z., Jin, P., and Ning, D. Z. (2023a). Power generation and wave attenuation of a hybrid system involving a heaving cylindrical wave energy converter in front of a parabolic breakwater. *Energy* 282, 128364. doi:10.1016/j.energy.2023.128364

Zhou, B. Z., Zheng, Z., Hua, J. J., Lin, C. S., Jin, P., Wang, L., et al. (2023b). Annual performance and dynamic characteristics of a hybrid wind-wave floating energy system at a localized site in the North Sea. *Ocean. Eng.* 280, 114872. doi:10.1016/j.oceaneng.2023.114872